Biophysical Chemistry 158 (2011) 61–72

Contents lists available at ScienceDirect

Biophysical Chemistry

journal homepage: http://www.elsevier.com/locate/biophyschem

Influence of the conserved active site residues of histidyl tRNA synthetase on the mechanism of aminoacylation reaction

S. Dutta Banik, N. Nandi *

Department of Chemistry, University of Kalyani, Kalyani, Nadia, West Bengal, 741235, India

ARTICLE INFO

Article history:
Received 29 March 2011
Received in revised form 3 May 2011
Accepted 3 May 2011
Available online 12 May 2011

Keywords:
Aminoacylation
Active site
Aminoacyl tRNA synthetase
Reaction mechanism
ONIOM calculation

ABSTRACT

The relation between the conservation of active site residues and the molecular mechanism of aminoacylation reaction is an unexplored problem. In the present paper, the influences of the conserved active site residues on the reaction mechanism as well as the electrostatic potential near the reaction center are analyzed for Histidyl tRNA synthetase from *Escherichia coli*, *Thermus thermophilus* and *Staphylococcus aureus*. While the primary structures show both convergence as well as divergence, the secondary level structures of the active sites of the three species show considerable conservation in the respective structural organizations. The conserved active site residues near the reaction center, which have a major role in the reaction mechanism and catalysis, retain their specific position and orientation relative to the substrate in the three species. In order to understand the influence of different conserved and nonconserved residues near the reaction center, two different models are considered. First, a large model of active site with the substrates, Mg^{2+} ions and water is constructed in which the first shell residues (including both conserved as well as nonconserved) near the reaction center are studied. From the large model, a smaller model is constructed for reaction path modeling individually for three species. Validation of the smaller model is carried out by comparing the energy surfaces of large and small models as a function of reaction coordinates. Further, the electrostatic potential near the reaction center for the large and small model are compared. The transition state structures of the activation step of aminoacylation reaction for *E. coli*, *T. thermophilus* and *S. aureus* are calculated using the combined *ab-initio*/semi-empirical calculation. The similarity of the energy profiles as a function of the relevant reaction coordinate and the orientation of the catalytic residue, Arg259, indicate that the reaction mechanisms are identical which are guided by the strikingly similar structural pattern formed by conserved residues for three species. The energy surfaces have close resemblance in three species and present a clear perspective that how the reaction proceeds with the aid of different conserved residues. The study of electrostatic potential confirms this view. The present study provides an understanding of the relationship between the conservation of residues and the efficient reaction mechanism of aminoacylation reaction.

1. Introduction

Aminoacylation reaction is a key step of the multistep protein synthesis and is a vital life process. In this reaction a given amino acid is attached to its cognate tRNA which is a prerequisite for the subsequent peptide bond formation. The reaction is catalyzed by the aminoacyl tRNA synthetase (aaRS) and occurs via two steps, namely amino acid activation and tRNA charging. Different aspects of these two steps are studied in detail [1–15].

Similar to the other classes of enzymetic reactions, aminoacylation reaction occurs within the active site of aaRS. The active site which is a cavity or cleft is the closest vicinity of the reactants within an enzyme, such as aaRS. The different regions of the active site and its composing residues enclose the reactants, locate them in the proximal position as well as orientation suitable for the reaction. Architecture of the active site and the chemical properties of the active site residues therein are responsible for the recognition and the substrate specificity and most importantly catalyzing the reaction. The preorganized electrostatic environment of the active site is the origin of the catalytic power of the enzyme [16]. The active site residues not only form a perfectly complimentary binding pocket for the substrates but also carry the reactants to the product state via the transition state. Computational studies of few aaRSs have revealed diverse roles of these residues such as recognition of the substrates, positioning of the substrates, chiral specificity and catalysis [11–15].

However, the correlation between the presence of a specific and conserved active site residue in a particular aaRS of different species and its influence on the mechanism of aminoacylation reaction is not understood. Do the conserved residues which are the nearest neighbors to the substrates in the organized active site structure guide the reaction in an efficient way? To understand this issue it is necessary to look into the molecular detail of the active site of a given

* Corresponding author. Fax: +91 33 25828282.
E-mail address: nilashisnandi@yahoo.com (N. Nandi).

0301-4622/$ – see front matter © 2011 Elsevier B.V. All rights reserved.
doi:10.1016/j.bpc.2011.05.006

aaRS from different organisms and its interaction with the substrate molecules. The substrate molecules involved in the aminoacylation reaction are ATP, amino acid and tRNA. The molecular fragments of ATP and amino acid are the adenosine group, the ribose sugar, the triphosphate group bearing negative charge (belongs to ATP), the positively charged amino group, the negatively charged carboxylic acid group (in the zwitterionic form of the amino acid) and the side chain (except in the case of glycine, which has no side chain). The side chain differs in polarity, charge or hydrophobicity for 20 amino acids and may contain a functional group (positively or negatively charged or polar) adding further diversity to the nature of the substrate. In corroboration with the chemical structure of the foregoing groups of the substrates, the active site residues of the corresponding aaRS have complementary chemical structure so that favorable interactions can bind the substrates effectively and with high fidelity. This complementary nature of the interaction between the substrate and the active site must be responsible for the efficiency of the reaction. However, quantitative understanding of such principles is not yet available.

As the active site residues and their architectonics control the mechanism of different steps of the reaction, it is obvious that the structural pattern of the active site (composed of amino acids) of aaRSs is developed and optimized through the evolutionary pathway to make the process of protein synthesis as error-free. The evolved structural arrangement, efficient to carry out the reaction accurately, is conserved thereafter or possibly continuing to develop. The enzyme superfamilies exhibit remarkable variations in substrate specificity, reaction chemistry as well as catalytic residues [17]. Consequently, to follow the correlation between the conservation of active site residues and the molecular mechanism of a particular reaction in different species is a complex problem. On the other hand, a look into the crystallographic and biochemical studies revealed that a number of active site residues are conserved in different species for a given aaRS [1–10]. It is tempting to conclude that the nonconserved residues might have roles which are either less significant or different from the roles that are influencing the reaction mechanism and/or catalytic activity. Obviously, the related understanding has utility in the development of novel designer biocatalysts.

An electronic structure based analysis of the aminoacylation reaction in different species is necessary to understand the influence of various active site residues on the progress of the reaction. It is further necessary to follow the electronic structure based analysis of the transition state and calculation of the energy surface based on the crystal structure of aaRS from different species. Such comparative study for any aaRS is unavailable at present to the best of our knowledge. A possible limitation could be due to the large computational time required, remembering that the application of quantum chemical method is limited by the system size [18]. Significant insight can be obtained into the reaction mechanism by identifying the relevant coordinate manifold [19–21]. Among the three regions of active site namely, ATP binding pocket, the amino acid binding pocket and the intervening region close to the carboxylic acid group of His and the α-phosphate group of ATP, the later region is closest to the segments of the substrates which undergo most significant reorganization characteristic of the reaction [22]. The intervening region has foremost importance in the progress of the reaction. Since the residues of the intervening region closest to the reaction center (close to the ester linkage) are proximal to the reacting fragment of amino acid and ATP, it is essential to consider them to study the reaction mechanism of the aminoacylation reaction.

The active site constitutes only a small part of the enzyme and the influence of the remaining distant regions of the macromolecule on the catalytic mechanism is nonnegligible. However, the interaction of the nearest neighbors with the substrates have dominant influence on the mechanism of enzymatic reactions due to $(1/r^n)$ dependence of interactions of electrostatic origin, where the power (n) depends on the nature of the interaction. Parallel to this notion, it is known that mutations close to the active site can enhance enantioselectivity [23]. Since protein's local structure and dynamics are coupled with the longer length scale structure and dynamics, the active site structure and dynamics are correlated with the structure and motion of the higher level (secondary or tertiary level). However, the basic reaction mechanism and fidelity is expected to be dependent on closer residues rather than the influences from distant residues.

With this end in view, we first compared the primary and secondary structures of HisRS from three different organisms (*Escherichia coli*, *EC*; *Thermus thermophilus*, *TT* and *Staphylococcus aureus*; *SA*) with a focus on the respective active site structures. In order to understand the influence of conserved and nonconserved active site residues near the reaction center two different models of active site are considered. First, a large model of the active site with the substrates, Mg^{2+} ions and water is constructed in which the first shell residues near the reaction center are included. From the large model, a smaller model is constructed, in which the residues essential for reaction path modeling, Mg^{2+} ions and water are retained. Validation of the smaller model is carried out by comparing the energy surfaces of large and small models as a function of reaction coordinates. Further, the electrostatic potential (ESP) near the reaction center for the large and small model are compared for each species. The influences of different active site residues on the reaction path as well as the electrostatic potential near the reaction center are analyzed for HisRS of *EC*, *TT* and *SA*. The reaction mechanism is quantitatively analyzed using electronic structure based methods. The transition state geometries of the activation step of aminoacylation reaction for *EC*, *TT* and *SA* are calculated using the combined *ab-initio*/semi-empirical method. The activation energy barrier is computed using the Polarizable Continuum Model (PCM). The energy surfaces related to the change from the reactant to the product via the transition state as a function of the relevant reaction coordinate and orientation of the catalytic residue Arg259 (as per numbering scheme in HisRS of *EC* and the corresponding numbering sequence in HisRS of *TT* and *SA* are given in Table S1 of the supporting information) are computed. The details of the calculation are presented in the following section.

2. Computational methods

The primary and secondary structures of HisRS for three prokaryotic species, *EC* (1KMM.PDB and 1KMN.PDB) [24], *TT* (1ADJ.PDB and 1ADY.PDB) [25] and *SA* (1QE0.PDB) [26] are compared with a focus on the respective active site structures. Based on the primary sequences of the HisRS of *EC*, *TT* and *SA*, similarities and dissimilarities in the respective primary sequences are compared (Fig. 1). The residues 1–325 belong to the catalytic domain of HisRS [3] and active site is constituted by this domain. Fig. 1 shows that within this catalytic domain more than 30% residues are conserved in the three organisms. This is consistent with the literature data [26]. More specifically, motifs and loops (such as motif II (103–134), motif III (299–319), HisA loop (257–264); numbering scheme is as in *EC*), either in close proximity to the reaction center or involved in the formation of active site show more similarity in sequence than the other parts of the catalytic domain. Despite this sequence similarity in the catalytic domain, diversities are observed in the domains and loops which are relatively far from the reaction center.

The common features of the secondary structures (the arrangements of the anti-parallel β-sheet and α-helices) of the active sites for the HisRS of *EC*, *TT* and *SA* are shown in Fig. 2(a–c), respectively. The separation between different conserved active site residues are shown for the three species in Fig. S1(a–c), respectively. Comparison of the molecular organization of the first shell active site residues of HisRS in *EC*, *TT* and *SA* are shown in Fig. S2(a–c). The structures indicate that

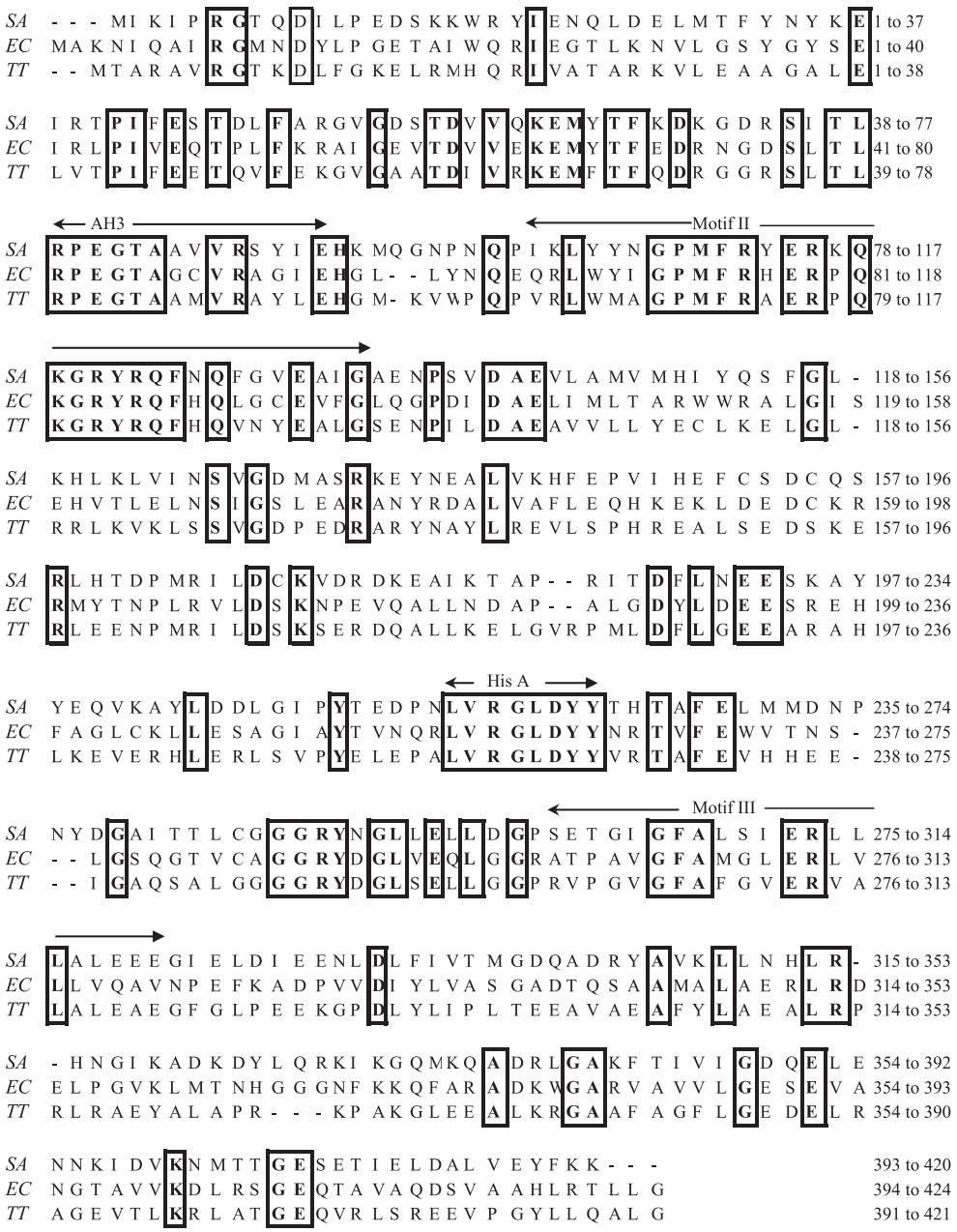

Fig. 1. Sequence alignments of three prokaryotic HisRS synthetase for EC [24], TT [25] and SA [26]. The various loops and motifs are shown by arrows. The residues conserved among the three species are enclosed by boxes and bold letters.

the active site wall of HisRS in the vicinity of the reactants is composed of both conserved and nonconserved residues in all three cases.

It is essential to consider the residues at the intervening region to model the reaction mechanism as mentioned in the Introduction. Among the conserved residues near the reaction center, Arg259 has catalytic role [14]. This residue is indispensable for the reaction and the residue is conserved in *EC*, *TT* and *SA*. The conserved Arg113 has a role in charge neutralization which reduces the electrostatic potential of phosphate group of ATP is essential for the progress of the reaction. The Glu83 responsible for the placement of His via favorable interaction with amino group of His and is conserved. Pro82 and Gly84 make the conformation of the peptide chain turned in such a way that the side chain of intervening Glu83 is projected towards the reaction center. Proline residue (Pro82 in HisRS) is known to be responsible for creating a turn [27]. The Gly (Gly84, in HisRS) is a highly conformationally flexible residue is also observed in a turn. These two residues are also conserved. Gln127 form hydrogen bond with the ribose sugar ring of ATP as well as carboxylic group of His and is conserved. The Ala306 and Gly84 have van der Waals interaction with the nonpolar part of His and are conserved in three species. The Gly260 and Leu261 form a hydrophobic patch which is close to the nonpolar region of His (close to the chiral center of His denoted as C^*). Both of these residues are conserved. The Ala284 is close to the C^* and is nonconserved (a Gly is present in *TT* and *SA* instead of Ala). The polar side chain of Thr60 is at the remote side of the wall near the ATP and is conserved. The Val62 (having a nonpolar side chain) is nonconserved and is replaced by Ile (in *TT*) which also has a nonpolar side chain. In many cases, the influence of nonconservation on the reaction mechanism and catalysis is expected to be low as the peptide linkage corresponding to the nonconserved residue is relatively closer to the reaction center. The linkage has invariant structure and is not dependent on whatever variation occurs in the nature of the side

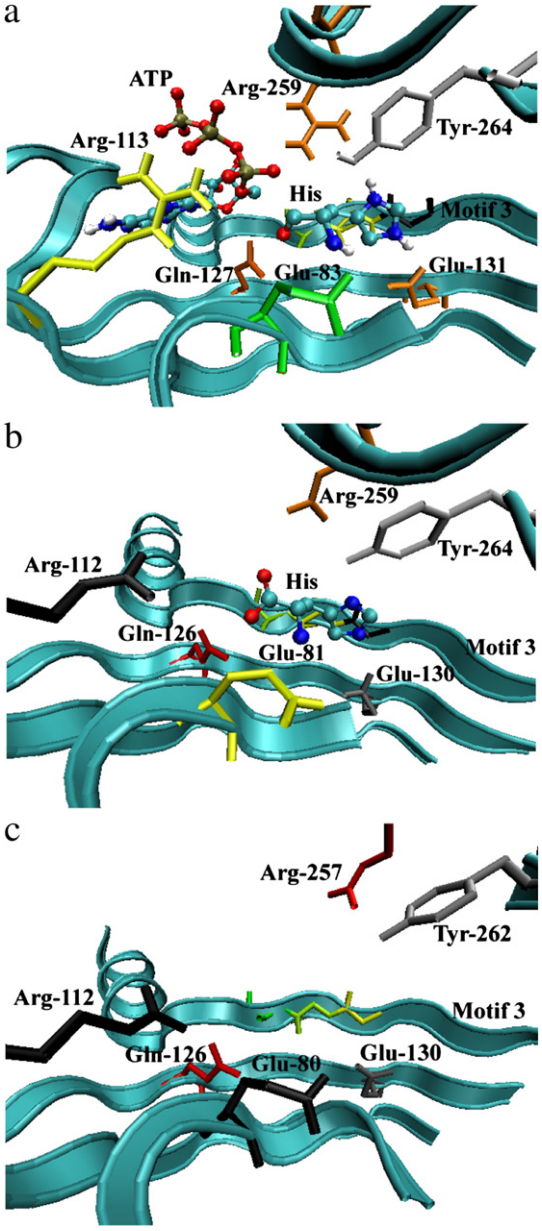

Fig. 2. The representation of the active site of three prokaryotic HisRS (a) EC [24], (b) TT [25] and (c) SA [26] as obtained from the respective crystal structures. The images are prepared using VMD [51].

chain. In such cases, the side chain of the nonconserved residues being relatively far from the reaction center, their influence is expected to be less compared to the conserved ones.

To analyze the influence of the active site residues (conserved and nonconserved) of HisRS of *EC*, *TT* and *SA*, near the reaction center, two models are considered. Three dimensional representations as well as schematic representations of the models and how they are prepared from the crystal structure are shown in the Fig. S3 (a–c) and S4 (a–c) in the supporting information, respectively. The first model includes all the foregoing twelve amino acids (Thr60, Val62, Pro82, Glu83, Gly84, Arg113, Gln127, Arg259, Gly260, Leu261, Ala284 and Ala306), two Mg^{2+} ions, two water molecules (present in the crystal structure) and substrates. The model is termed as $Model^{EC/TT/SA}_{Reactant(large)}$. To generate the model structures of reactant for *EC* (namely, $Model^{EC}_{Reactant(large)}$ and $Model^{EC}_{Reactant}$) from the crystal structure of HisRS of *EC* [24], the $-CH_2OH$ group of the histidinol moiety is replaced by the carboxylic acid group. Details are mentioned in the section A of the supporting information. To prepare the $Model^{TT}_{Reactant(large)}$ and $Model^{TT}_{Reactant}$, the ATP is modeled in the crystal structure of HisRS [25] of *TT* complexed with histidine. The $Model^{SA}_{Reactant(large)}$ and $Model^{SA}_{Reactant}$ are generated from the crystal structure of HisRS [26] from *SA* and the histidine and ATP is modeled by superimposing the 1KMN.PDB and 1QE0.PDB. The schematic representations of the models of *EC*, *TT* and *SA* are shown in Fig. 3(a–c).

It is not computationally feasible to include all atoms of the enzymatic structure into *ab-initio* level of theory. It is possible to use hybrid computational models including *ab*-initio, semi-empirical and molecular mechanics [28,29] as well as to reduce the number of atoms which are essential to model the reaction chemistry and catalytic activity [30] systematically and correctly. The combined quantum mechanical/molecular mechanical approach has recently received attention as applied to larger systems [28,29]. Optimization of macromolecular system is relatively faster in the multilevel hybrid method such as multilayered ONIOM model (abbreviation of the title "*our n-layered integrated molecular orbital and molecular mechanics*" as used by the developers) [31–33]. Calibration studies have demonstrated that the resulting predictions are essentially equivalent to those that would be produced by the high accuracy method alone on the entire molecule [31–37]. Since the focus of the present work on the reaction mechanism, which is dependent on the electronic rearrangements in the close vicinity of the reactants, application of *ab-initio* level around the substrates and medium level of theory (semi-empirical) beyond this region is appropriate. Multilayered ONIOM method is used to optimize the structures. *Ab-initio*, semi-empirical and molecular mechanics are applied. In all calculations, link hydrogen atoms are added to the MM-bonded QM atoms to saturate the valence orbital of the QM subsystem [34]. The method of mixing different quantum mechanical/semi-empirical method in ONIOM calculation is important. The ONIOM mixing different quantum mechanical/semi-empirical (QM/SE) method is an improvement over the hybrid quantum mechanical/molecular mechanical (QM/MM) methods [38]. For large reactive systems, the calculation of energies can be simplified by treating the active part with a high-level quantum mechanical (QM) (*ab-initio* or density functional) approach and the environment with a less sophisticated semi-empirical (SE) approach [38].

We have used free optimization of the models of active site using both ONIOM (HF/6-31G*:PM3) and ONIOM (B3LYP/6-31G*:PM3) methods to prepare the reactant state. The optimized geometries of the reactant state using two different levels of theories are compared. The result shows that both the *ab-initio* as well as density functional theory gives almost identical optimized state of reactant. The average deviation in the position of the respective atoms in the optimized geometries using different level of theories is 0.15 Å. As indicated in the literature, it is not computationally feasible, to include all atoms of the crystallographic structure, it is customary to reduce the number of atoms which are essential to model the reaction chemistry and catalytic activity [30]. We have verified the accuracy of basic model by systematically analyzing the reduction of system size, using a large and small model. However, in order to consider the effect of the rest of the enzyme, the activation energy barrier is computed using Polarizable Continuum Model (PCM) model of low dielectric solvent [39].

Three level ONIOM (HF/3-21G: PM3: UFF) method is used to optimize the $Model^{EC/TT/SA}_{Reactant(large)}$. The carboxylic acid group of His, α-phosphorus atom of ATP with attached oxygen atoms and the guanidinium group of Arg113 and Arg259 are included in the *ab-initio* level of theory. Remaining parts of the substrate moieties and the active site residue Glu83 and Gln127 as well as two water molecules and two Mg^{2+} ions are considered at medium level (semi-empirical; *Parameterization 3 of MNDO* or PM3) [36] and all the remaining atoms of the surrounding residues are considered at lower level (molecular

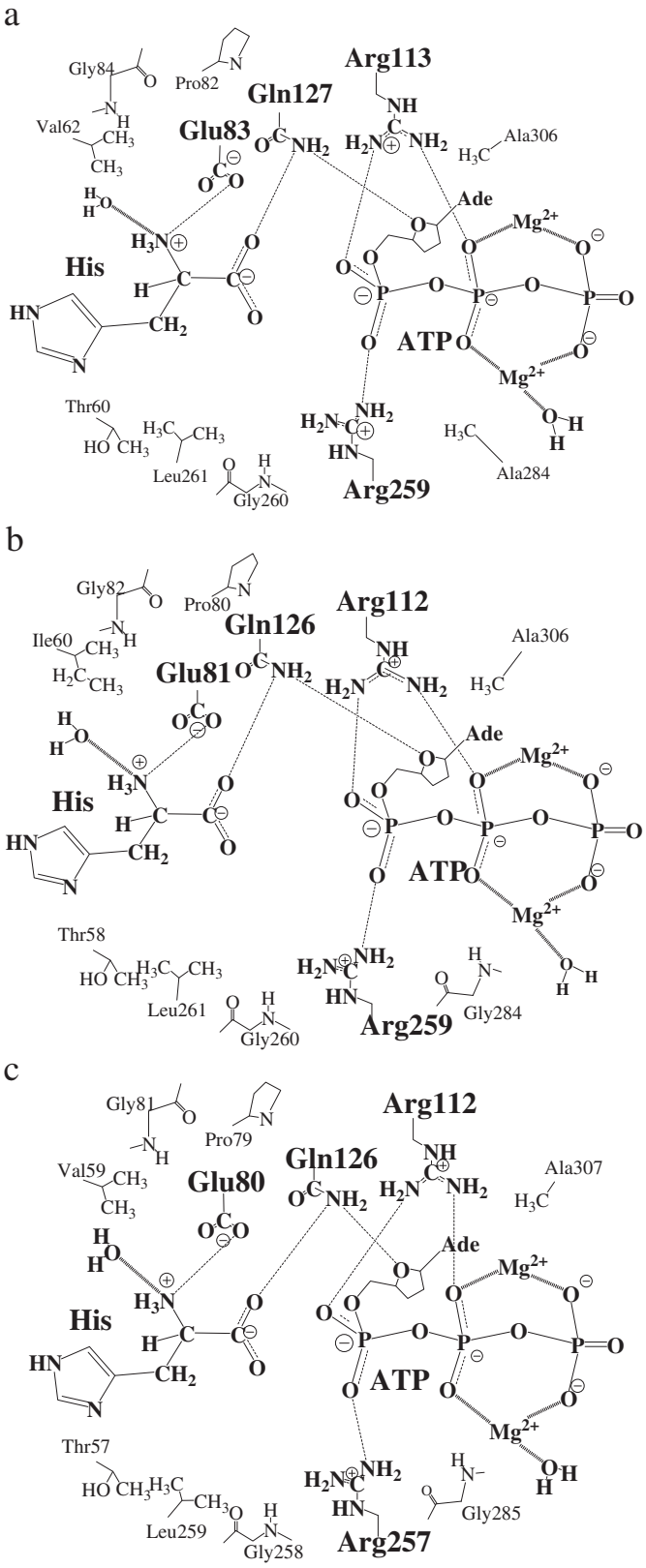

Fig. 3. The schematic representation of the (a) $\text{Model}^{\text{EC}}_{\text{Reactant(large)}}$ (b) $\text{Model}^{\text{TT}}_{\text{Reactant(large)}}$ and (c) $\text{Model}^{\text{SA}}_{\text{Reactant(large)}}$ showing the interaction between the substrates molecules (His and ATP) and the active site residues near the reaction center only. The residues near the His and ATP are not shown as discussed in the theoretical section. Nonbonded interactions (such as electrostatic and hydrogen bonding) between the active site residues and substrates are shown by dotted line. The Mg^{2+} ions bound with ATP and two water molecules (near the Mg^{2+} ion and the α-amino group of His) are also shown. The active site residues considered in the $\text{Model}^{\text{EC/TT/SA}}_{\text{Reactant}}$ are indicated in bold.

mechanics; *Universal Force Field* or UFF) [37]. The Cartesian coordinates of the atoms of the optimized $\text{Model}^{\text{EC/TT/SA}}_{\text{Reactant(large)}}$ are given in Table S2 (a–c) of supporting information.

The second model (namely, $\text{Model}^{\text{EC/TT/SA}}_{\text{Reactant}}$) is a smaller model of active site which contains the residues which are essential for the reaction. This includes Glu83, Arg113, Gln127 and Arg259 active site residues, two Mg^{2+} ions, two water molecules as well as the substrate amino acid (His) and ATP. Total number of atoms present in the smaller model is 100. The nonpolar active site residues Val62, Pro82, Gly84, Gly260, Leu261, Ala284 and Ala 306 as well as polar Thr60 of the intervening region are excluded in this model. As these residues are relatively far from the reaction center compared to the Glu83, Arg113, Gln127 and Arg259, it is expected that they play a less significant role in the reaction mechanism. Further, these residues interact with the substrates via weak hydrogen bonding interaction, dipolar interaction or van der Waal interaction which are weaker interactions than charge-charge type and the influences of the residues are expected to be less significant. The exclusion of these residues is validated based on ESP and energy surface of small and large model as described in the following paragraph. The smaller model structures are optimized using two level ONIOM (HF/6-31G*: PM3) method. The carboxylic acid group of His, α-phosphorus of ATP with attached oxygens and the guanuidinium group of Arg113 and Arg259 are included in the *ab-initio* level of theory. Remaining atoms of the reactant and surrounding residues are considered at semi-empirical level. The Cartesian coordinates of the atoms of the optimized $\text{Model}^{\text{EC/TT/SA}}_{\text{Reactant}}$ are given in Table S3 (a), Table S4 (a) and Table S5 (a) of supporting information, respectively.

Validation of the smaller model is carried out in two ways. First, the variation of energy of the reactant state as a function of relevant reaction coordinate as well as the orientation of the Arg259 (major catalytic residue) is compared for the optimized structures of $\text{Model}^{\text{EC/TT/SA}}_{\text{Reactant(large)}}$ and the $\text{Model}^{\text{EC/TT/SA}}_{\text{Reactant}}$, respectively. During the progress of the reaction, the reactant state undergoes structural rearrangement. The corresponding energy surface of the smaller model must corroborate with that of the large model. The first variable is a composite variable which describes the approach of the reactants towards each other and the other one considers the effect of the influence of the major catalytic residue, Arg259. Explicitly, the composite variable is a reaction coordinate, q which describes the attack of the carboxylic acid group of His to the α-phosphorus atom of ATP and simultaneous breaking of the P–O (linked with β-phosphorus atom) bond leading to the inversion of the α-phosphorus atom of ATP. Thus $q = r_{P-O(PPi)} - (r_{P-O(His)} + r')$ where, the $r_{P-O(PPi)}$ is the relative separation between oxygen atom joining the α- and β-phosphorus atom of ATP and the α-phosphorus atom of ATP; $r_{P-O(His)}$ is the relative separation between the carboxylic oxygen atom of His and the α-phosphorus atom of ATP shown in Fig. 4. The r' is the projection of the αP–O_5' bond of ATP on the bond which is forming between the carboxylic oxygen atom of His and the α-phosphorus atom of ATP. During the progress of the reaction the magnitude of the $r_{P-O(PPi)}$ gradually increases and the magnitude of the r' decreases. As a result q increases as the reaction progresses towards the product state. The second variable measures the progress of the reaction as a function of the orientation of the catalytic residue Arg259 (denoted by Ω_{Arg}). The change in Ω_{Arg} is a measure of the influence of Arg259 on the reaction.

The variation of the interaction energy as a function of q and Ω_{Arg} for the optimized model of $\text{Model}^{\text{EC/TT/SA}}_{\text{Reactant(large)}}$ and $\text{Model}^{\text{EC/TT/SA}}_{\text{Reactant}}$ are studied using the ONIOM method as shown in Figs. 5(a–c) and 6(a–c), respectively. The three level ONIOM (HF/3-21G: PM3: UFF) method is applied for the optimized $\text{Model}^{\text{EC/TT/SA}}_{\text{Reactant(large)}}$ and the two level ONIOM (HF/6-31G*:PM3) method is applied for $\text{Model}^{\text{EC/TT/SA}}_{\text{Reactant}}$. Comparison of the energy profiles of large models and small models of *EC*, *TT* and *SA* as well as comparison of the energy profiles of *EC*, *TT* and *SA* are shown in Fig. 7(a–c) and Fig. 8(a, b), respectively.

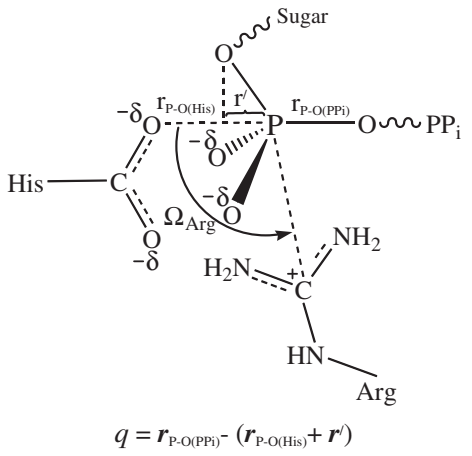

Fig. 4. The schematic representations of the reaction coordinate used to generate the energy surfaces of the reactant state, product state and the transition state. The $r_{P-O(His)}$ represents the relative separation between carboxylic oxygen atom of His and the α-phosphorus atom of ATP. The $r_{P-O(PPi)}$ represents the relative separation between α-phosphorus atom and oxygen atom joining the α- and β-phosphorus atom of ATP and r' represents the projection of the α P–O_5' bond of ATP on the forming bond that is r' (carboxylic oxygen atom of His and the α-phosphorus atom of ATP). Ω_{Arg} is the orientation of the catalytic residue Arg259 which is changed during the reaction. For detail see the text.

The electrostatic potential, $V(\vec{r})$ at a point $\vec{r}$ in space due to the electrons and nuclei of a molecule is given by

$$V(\vec{r}) = \sum_A \frac{Z_A}{\left|\vec{R_A} - \vec{r}\right|} - \int \frac{\rho(\vec{r'})d\vec{r'}}{\left|\vec{r'} - \vec{r}\right|} \quad (1)$$

Here, Z_A is the charge of the nucleus A located at $\vec{R_A}$ and the electronic density function of the molecule is $\rho(\vec{r})$. The details are given in section B of the supporting information. Generally, the positive potential due to an electrophile is far less than the positive potential of the nuclei. Therefore, the identification of the electrophilic center is relatively complex from the contour plot of ESP. On the other hand the negative potential value on the ESP contour plot indicates the presence of a nucleophile. The electronic rearrangement related to the attack of a nucleophile at an electrophilic center is favorable when one or more regions of negative potential is noted between the two species due to the presence of the nucleophile [40,41]. Further detail of one can define electrophilic and nucleophilic regions based on ESP maps are provided in the supporting information. The ESP near the reaction center is computed for both large and small models for further validation of the small model. The optimized structures of $\text{Model}^{EC/TT/SA}_{Reactant(large)}$ and the optimized structures of $\text{Model}^{EC/TT/SA}_{Reactant}$ are used to compare the electrostatic potential. In both cases, the ESP are computed using HF/6-31G* level of theory. The presence of a region of negative potential is noted between the ATP and His for $\text{Model}^{EC/TT/SA}_{Reactant(large)}$. The corresponding ESP contour plots are shown in Fig. 9(a–c), respectively. The influence of the active site residue Arg113 and the orientation of the carboxylic acid group of His on the lowering of ESP at the intervening region are also studied. The related ESP plots are shown Fig. S5(a–c) and S6(a, b), respectively. All ESP plots are generated using HF/6-31G* level of theory.

We also carried out ONIOM (MP2/6-31G*:PM3//HF/6-31G*:PM3) level calculation of the transition state geometry of the activation step of HisRS for *EC*, *TT* and *SA*. The QST3 method is used for transition state calculation. The transition state geometries of the *EC*, *TT* and *SA* species are shown in Fig. 10(a–c), respectively. The mode of vibration that corresponds to the imaginary frequency is calculated for the three organisms to identify the transition state. The Cartesian coordinates of the atoms of the optimized models of reactant, transition state and product for *EC*, *TT* and *SA* are given in the Table S3 (a–c), Table S4 (a–c) and Table S5 (a–c) of supporting information, respectively. The energy profiles corresponding to the progress of the reaction are studied in

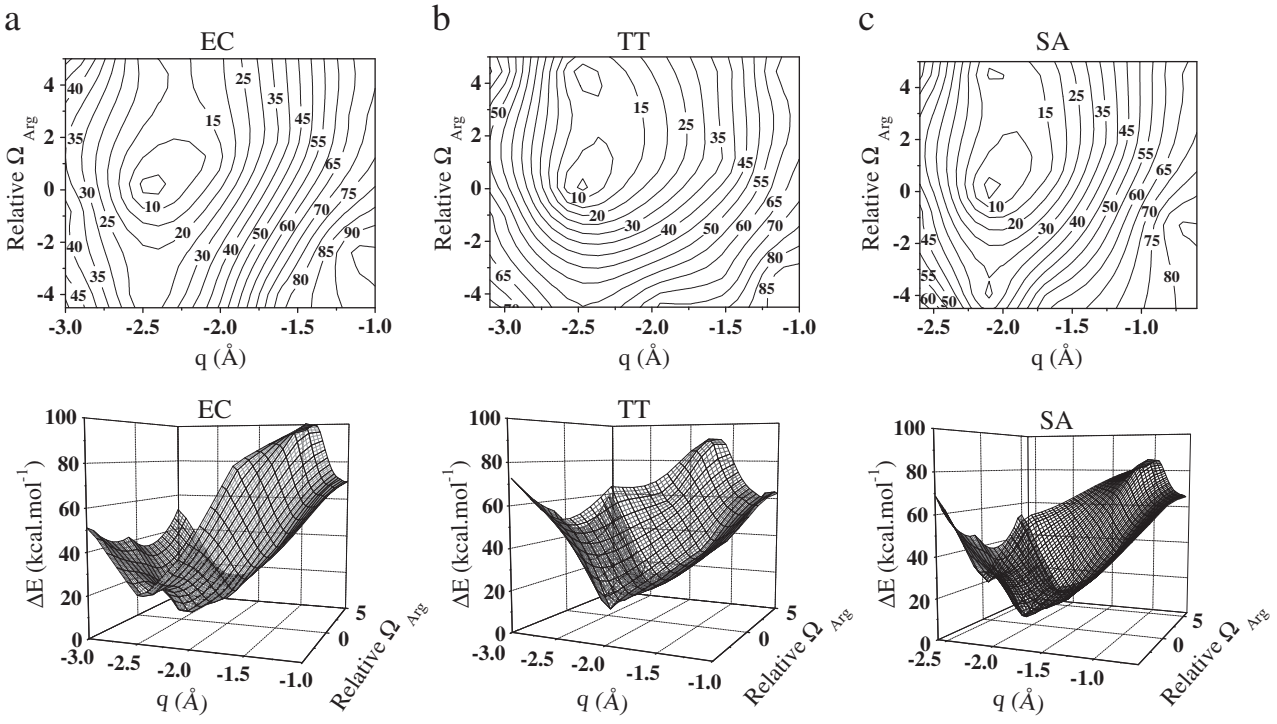

Fig. 5. The variation of interaction energy as a function of q (as shown in Fig. 4) and relative orientation of the catalytic residue Arg259 (Ω_{Arg}) with respect to the optimized reactant for the optimized models (a) $\text{Model}^{EC}_{Reactant(large)}$, (b) $\text{Model}^{TT}_{Reactant(large)}$ and (c) $\text{Model}^{SA}_{Reactant(large)}$ using three level ONIOM (HF/3-21G: PM3: UFF) method. The ΔE represents the relative energy with respect to the optimized reactant of the respective models in kcal.mol^{-1}. The Cartesian coordinates of the respective optimized models are given in Tables S2 (a–c) of the supporting information.

three species using $\text{Model}^{\text{EC/TT/SA}}_{\text{Reactant}}$ as a function of the q and Ω_{Arg}. The variation in energy is computed based on optimized models of the active site of the respective organisms using two level ONIOM (HF/6-31G*:PM3//HF/6-31G*:PM3) method. The corresponding three dimensional energy landscapes as well as two dimensional plots are shown in Fig. 11(a–c), respectively.

In order to compare the computed activation barrier using the present model with available experimental data, it is necessary to incorporate the effect of the overall enzyme structure surrounding the active site. This is considered by a low dielectric constant solvent representing the protein matrix as carried out in literature [42]. In the present work we used a continuum of low dielectric constant ($\varepsilon = 4.335$) to represent the effect of the protein matrix surrounding active site and calculated the energies of the reactant, product and transition state using a Polarizable Continuum Model (PCM) model [39] at the HF/6-31G* level of theory). The Gaussian 03 suite of programs [43] is used for all calculations. The results are described in the following section.

3. Results and discussion

The sequences of HisRS of *EC* [24], *TT* [25] and *SA* [26] are compared in Fig. 1. The sequence alignments show that only few residues out of approximately 400 amino acids in the primary structure are conserved and more residues are nonconserved in the complete amino acid sequence. Only a small percentage of amino acids are composing the wall of the active site. This is understandable as the active site constitutes only a small fraction of the overall enzyme structure. Despite the strong divergence in the primary structure, the higher level structure constituting the active site region shows significant conservation in the organizational features at smaller length scale as shown in Fig. 2(a–c). The conserved residues such as Thr60, Pro82, Glu83, Gly84, Arg113, Gln127, Arg259, Gly260, Leu261, and Ala 306 constituting the intervening region of the active site are already noted in the computational methods section. The common structural features constituting the active site in the three species are as follows (based on crystallographic studies). The active sites are built on an anti-parallel β-sheet surrounded by α-helices. Both motif II and motif III contain conserved Arg residues and form a part of the active site. The Arg113 of motif II interacts with the α-phosphate group of ATP. The ATP is cradled by anti-parallel β-sheet formed by motif II and motif III. The adenine base stacks over a Phe and is fixed by the backbone portion of the motif II loop.

Fig. S1(a–c) shows that the organization of the higher level structure of the active site is such that various conserved active site residues are located in specific locations relative to the reactants, despite the gaps or divergence in the primary sequence. For example, the relative separations between the active site residues Glu83 and Arg113 are 8.76 Å, 8.70 Å and 8.35 Å while that between the Arg259 and Ala306 are 12.37 Å, 12.26 Å and 15.04 Å for *EC*, *TT* and *SA*, respectively. It may be noted that the larger separation between the Arg259 and Ala306 in the active of *SA* is due to the open conformation of apo HisRS [26] (unbound with either histidine or ATP). The organization of the active site structures of three species shown in Fig. S2(a–c) indicates that the active site is composed of more conserved residues than nonconserved ones. The comparison of the nearest neighbor residues indicates that these residues have closely similar arrangements in three cases. This is shown in the schematic representations of the first shell neighbors present in the active sites near the reaction center of *EC*, *TT* and *SA*, respectively (Fig. 3(a–c)).

The variation of the energies of the reactant states of *EC*, *TT* and *SA* as a function of q and Ω_{Arg} are shown in Fig. 5(a–c) and Fig. 6(a–c), respectively for $\text{Model}^{\text{EC/TT/SA}}_{\text{Reactant(large)}}$ and $\text{Model}^{\text{EC/TT/SA}}_{\text{Reactant}}$ based on the respective optimized geometries. The comparison of the energy surfaces corresponding to $\text{Model}^{\text{EC/TT/SA}}_{\text{Reactant(large)}}$ and $\text{Model}^{\text{EC/TT/SA}}_{\text{Reactant}}$ for each species as shown in Fig. 7(a–c) indicates that the nature of the energy surfaces are not significantly affected as distant residues are removed from the large model. This indicates that the progress of the reaction is not significantly dependent of the residues such as Thr60, Val62, Pro82, Gly84, Gly260, Leu261, Ala284 and Ala306. The comparison of the energy surfaces of optimized $\text{Model}^{\text{EC/TT/SA}}_{\text{Reactant(large)}}$ for *EC*, *TT* and *SA* and optimized $\text{Model}^{\text{EC/TT/SA}}_{\text{Reactant}}$ for *EC*, *TT* and *SA* as shown in Fig. 8(a, b) indicate that the nonconserved residues (Val62 and Ala284) have less significant role in dictating the nature of the energy surface. Explicitly, the Val62 and Ala284 are present in the large model of the active site of *EC*, Ile60 and Gly284 are present in corresponding model of *TT* while Val59 and Gly285 are present in the corresponding model of *SA*. Despite the nonconservation of residues in the $\text{Model}^{\text{EC/TT/SA}}_{\text{Reactant(large)}}$, the energy surfaces are closely similar for three species, as shown in Fig. 8(a). This indicates that the nonconservation has little effect on the reactant states and conserved residues have dominant influence.

The ESP contour plots for optimized $\text{Model}^{\text{EC/TT/SA}}_{\text{Reactant(large)}}$ are shown in Fig. 9(a–c), respectively. The presence of the region of negative potential is expected for the favorable attack of the nucleophile (carboxylic oxygen of His) at the electrophilic center (α-phosphorous of ATP) and is noted between the carboxylic acid group of His and phosphate group of ATP. Lowering of electrostatic potential is observed for small models of the three species in the intervening region between the His and ATP. The corresponding ESP contour plots are shown in Fig. S5(a–c), respectively. Region of negative potential at the reaction center is noted for $\text{Model}^{\text{EC}}_{\text{Reactant}}$. Lowering of potential is noted in the optimized geometries of the $\text{Model}^{\text{TT/SA}}_{\text{Reactant}}$ but no negative regions are observed in the reaction center. Inspection of the $\text{Model}^{\text{EC/TT/SA}}_{\text{Reactant(large)}}$ and the crystal structure of *EC* indicates that the α phosphorus atom of ATP is in the plane containing the COO^- group of His while the guanidinium group of Arg113 is in a plane nearly perpendicular to the plane containing the COO^- group of His and close to the phosphate group of ATP. Due to the structural rearrangements in the optimized $\text{Model}^{\text{TT/SA}}_{\text{Reactant}}$ compared to the large model, the position and orientation of the COO^- group of His and guanidinium group of Arg113 are not identical in the $\text{Model}^{\text{TT/SA}}_{\text{Reactant(large)}}$ and $\text{Model}^{\text{TT/SA}}_{\text{Reactant}}$. As a result the ESP is not negative in the later. Reorganization of the COO^- group of His and the Arg113 in the optimized $\text{Model}^{\text{TT/SA}}_{\text{Reactant}}$ generates the negative potential at the respective reaction center as shown in the Fig. S6 (a, b), respectively. This indicates that the absence of negative potential in $\text{Model}^{\text{TT/SA}}_{\text{Reactant}}$ is not due to the removal of residues but due to the structural rearrangement related to the reorganization of COO^- group of His and the Arg113 after optimization. The plots in Fig. S5 (a–c) show the lowering of electrostatic potential near the reaction center in small model which is similar to that of the large model. Consequently, the energy surface as well as electrostatic potential confirms that the $\text{Model}^{\text{EC/TT/SA}}_{\text{Reactant}}$ can be used as a smaller model to study the reaction mechanism in comparison of the three species.

The optimized geometries of the transition states of the first step of aminoacylation reaction for *EC*, *TT* and *SA* using the $\text{Model}^{\text{EC/TT/SA}}_{\text{Reactant}}$ are shown in Fig. 10(a–c). The optimized geometries confirm that the reaction proceed through a penta-coordinated transition state for three organisms. The carboxylic oxygen atom of His approach towards the α-phosphorus atom of ATP, the energy of the system increases and reaches the maxima at the pentagonal transition state. The results also indicate that the HisRS from the different organisms like *EC*, *TT* and *SA* follow similar mechanism for the activation step of aminoacylation reaction. The normal mode of vibration corresponding to the imaginary frequency indicates that during the reaction the α-phosphorus atom of ATP undergoes inversion in configuration in all cases.

The comparison of the geometries of the reactant state, transition state and product state in three species confirms that the in-line displacement mechanism in which the oxygen atom of the carboxylic group of His attacks the α-phosphorus atom of ATP is common. In all

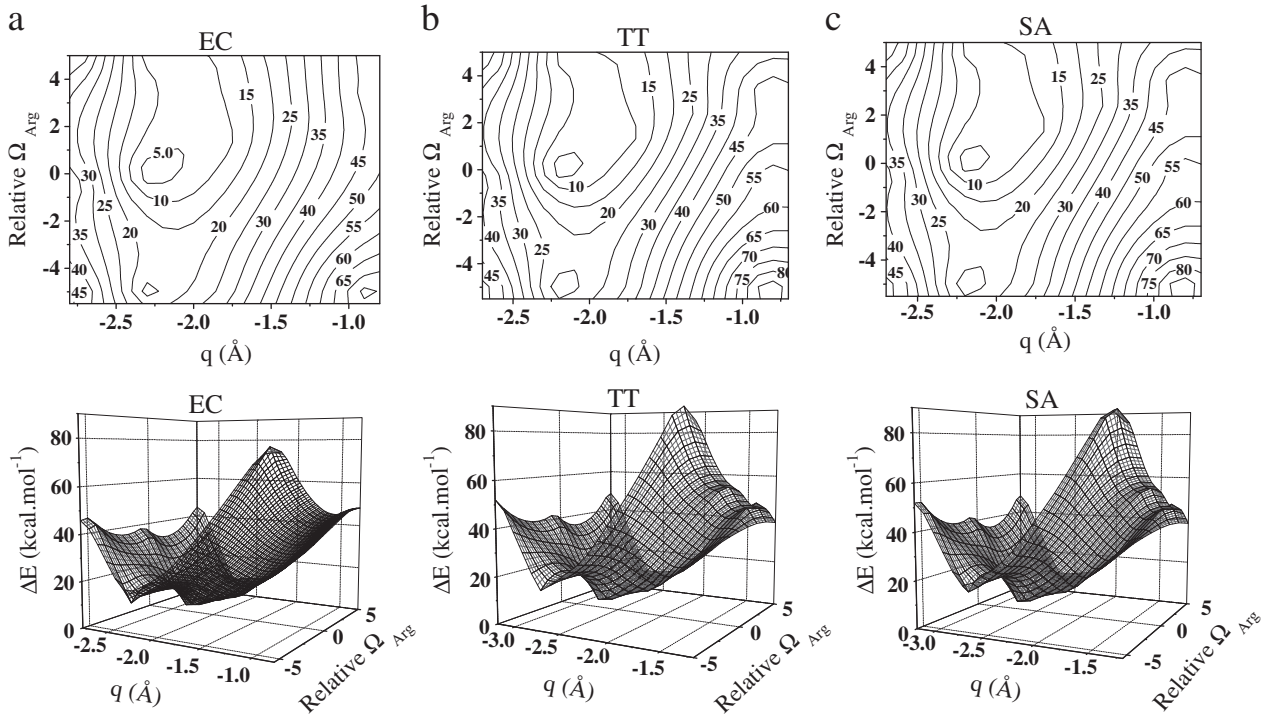

Fig. 6. The variation of interaction energy as a function of q (as shown in Fig. 4) and relative orientation of the catalytic residue Arg259 (Ω_{Arg}) with respect to the optimized reactant for the optimized models (a) $Model^{EC}_{Reactant}$, (b) $Model^{TT}_{Reactant}$ and (c) $Model^{SA}_{Reactant}$ using two level ONIOM (HF/6-31G*: PM3) method. The ΔE represents the relative energy with respect to the optimized reactant of the respective models in kcal.mol^{-1}. The Cartesian coordinates of the respective optimized models are given in Tables S3 (a), S4 (a) and S5 (a) of the supporting information, respectively.

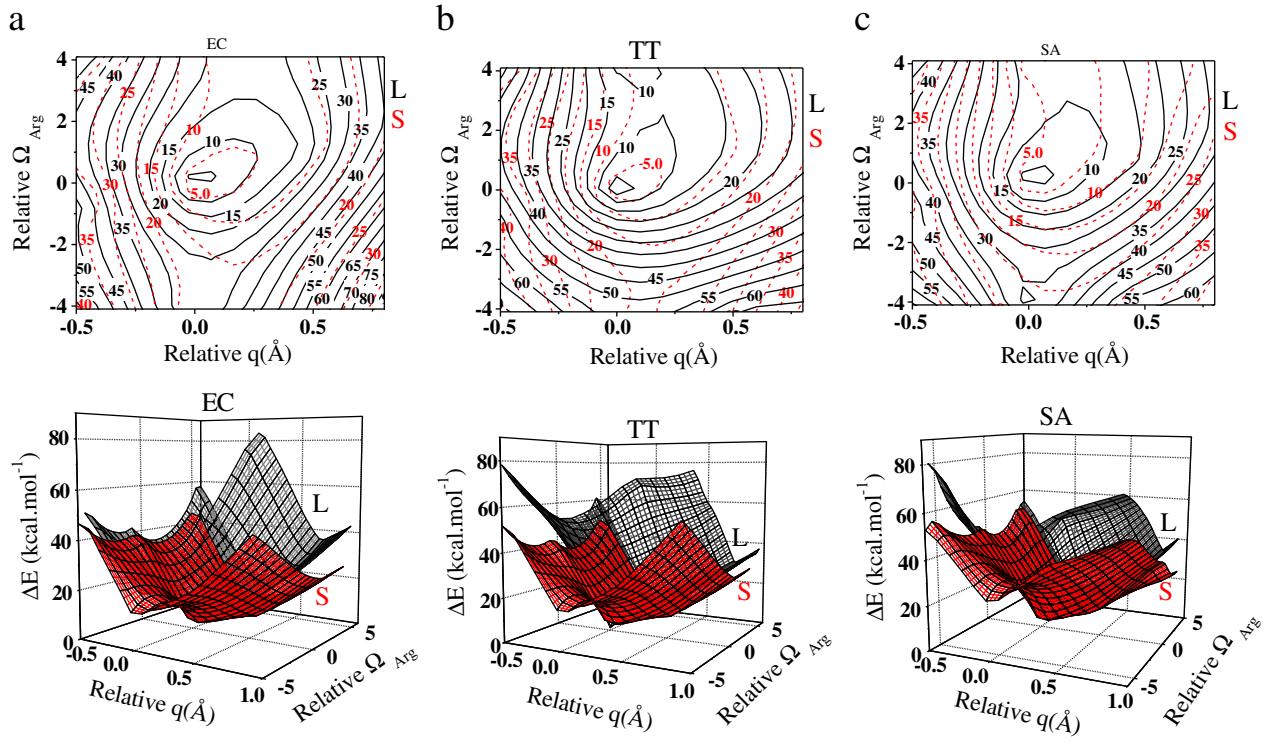

Fig. 7. Comparison of the variation of interaction energy as a function of relative q and relative orientation of the catalytic residue Arg259 (Ω_{Arg}) with respect to the optimized reactant for optimized models (a) $Model^{EC}_{Reactant(large)}$ (indicated by L) and $Model^{EC}_{Reactant}$ (indicated by S), (b) $Model^{TT}_{Reactant(large)}$ (indicated by L) and $Model^{TT}_{Reactant}$ (indicated by S) and (c) $Model^{SA}_{Reactant(large)}$ (indicated by L) and $Model^{SA}_{Reactant}$ (indicated by S) using ONIOM method. The relative q is the variation of q with respect to the value at the respective optimized models (taken as zero). The Cartesian coordinates of the optimized models are given in Tables S2 (a–c), S3 (a), S4 (a) and S5 (a) of supporting information.

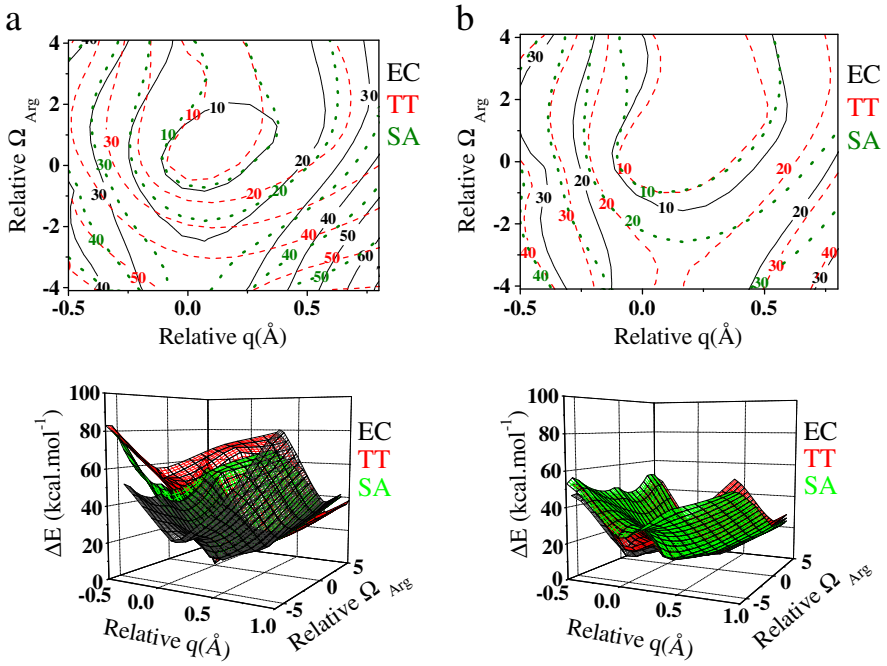

Fig. 8. Comparison of the variation of interaction energy as a function of relative q and relative orientation of the catalytic residue Arg259 (Ω_{Arg}) with respect to the optimized reactant for optimized models (a) $Model^{EC}_{Reactant(large)}$, $Model^{TT}_{Reactant(large)}$ and $Model^{SA}_{Reactant(large)}$ and (b) $Model^{EC}_{Reactant}$, $Model^{TT}_{Reactant}$ and $Model^{SA}_{Reactant}$ using ONIOM method. The relative q is the variation of q with respect to the value at the respective optimized models (taken as zero). The Cartesian coordinates of the optimized models are given in Tables S2 (a–c), S3 (a), S4 (a) and S5 (a) of the supporting information.

cases, the tetrahedral arrangement of the oxygen atoms (around the phosphorus atom) in the α-phosphate group inverts through a planar state in going from the reactant to the product state. This can be noted from a comparison of the bond angles and distances around the α-phosphate group in the optimized geometries of the reactant, transition state, and product. The results are described in Tables S6 (a) and Table S6 (b), respectively. The variations in the bond angles and distances in going from the reactant to the product via transition state demonstrate the attack of the carboxylic oxygen at the α-phosphorus atom and the concomitant inversion of oxygen attached with the α-phosphorus atom of ATP in *EC*, *TT* and *SA* respectively. The two C–O bond lengths of α carboxylic acid group of His are nearly same (a difference of 0.02 Å) in the reactant state which indicates that the negative charge is delocalized over the carboxylic oxygen atoms in the reactant state.

The distribution of electronic charge in the reactant state, transition state and product state are analyzed for three species. The Mulliken population analysis in the three species show that the negative charge over the carboxylic oxygen atoms gradually decreases. Simultaneously the negative charge over the oxygen atom of the leaving group increases on going from the reactant state to the product state. This indicates that the electron density is shifted from the carboxylic acid group of His to the oxygen atom of the leaving group in all cases. The features of the hydrogen bonding patterns of three species show close similarity as shown in the Table S7 of the supporting information. Despite the differences in the optimized structures of *EC*, *TT* and *SA*, the molecular mechanism is same.

The barrier height of the transition state using a PCM model at the HF/6-31G* level of theory is 13.03 kcal.mol^{-1}. The experimental activation energy is 14.5 kcal.mol^{-1} [24]. The region surrounding the active site is microhetereogeneous in nature and mimicking the same by a uniform low dielectric solvent is expected to be the source of the discrepancy between the computed and experimental data. The result indicates that a large part of the lowering of the activation barrier is arising from the active site residues. The energy barrier of the uncatalyzed reaction (without any active site residues and using a continuum of dielectric constant as 4.335) corresponds to 47.13 kcal.mol^{-1} as expected.

Further analysis of the progress of reaction is carried out based on the energy surface describing the reactant state, transition state and product state as a function of the reaction coordinate q as well as the orientation of the catalytic residue, Arg 259. This is shown in Fig. 11(a–c). The energy surfaces show two distinct deep minima at the lower left and upper right which correspond to the reactant and product states, respectively. These two states are separated by an energy barrier in three species. It is important to note that the optimized geometry of the transition state is located between the barriers separating the reactant and product state. The location of the transition state corresponds to the value of q as zero in all cases. The mutual proximity of the His and ATP (parameterized by q) changes significantly throughout the course of the reaction and is a natural choice of variable to describe the reaction path. Negative values of q indicate larger separation between His and ATP which corresponds to the larger values of $(r_{P-O(His)}+r')$ and corresponds to the reactant state. The positive q values indicate larger separation between the α-phosphate group of ATP and leaving group that is large value of $r_{P-O(PPi)}$ which corresponds to the product state. In all cases, the proximity of His and ATP decreases while that between the α-phosphate group of ATP and leaving group increases with the concomitant change in Ω_{Arg} in going from reactant state to the product state. The later state is a deeper minima than the reactant state.

The crystallographic [24] and recent quantum mechanical studies [14] suggested that the Arg259 plays an important catalytic role in the activation step rather than merely reducing the negative charge density over the ATP. The reaction path critically depends on the orientation of the Arg259 in all species as shown in Fig. 11(a–c). The orientation of the Arg259 changes with the progress of the reaction as this residue anchors the carboxylic acid group of His as well as the oxygen atom of the phosphate group of ATP in the reaction pathway as a catalytic process. Importantly, only certain ranges of orientations of the Arg259 are related with the favorable low energy pathway and

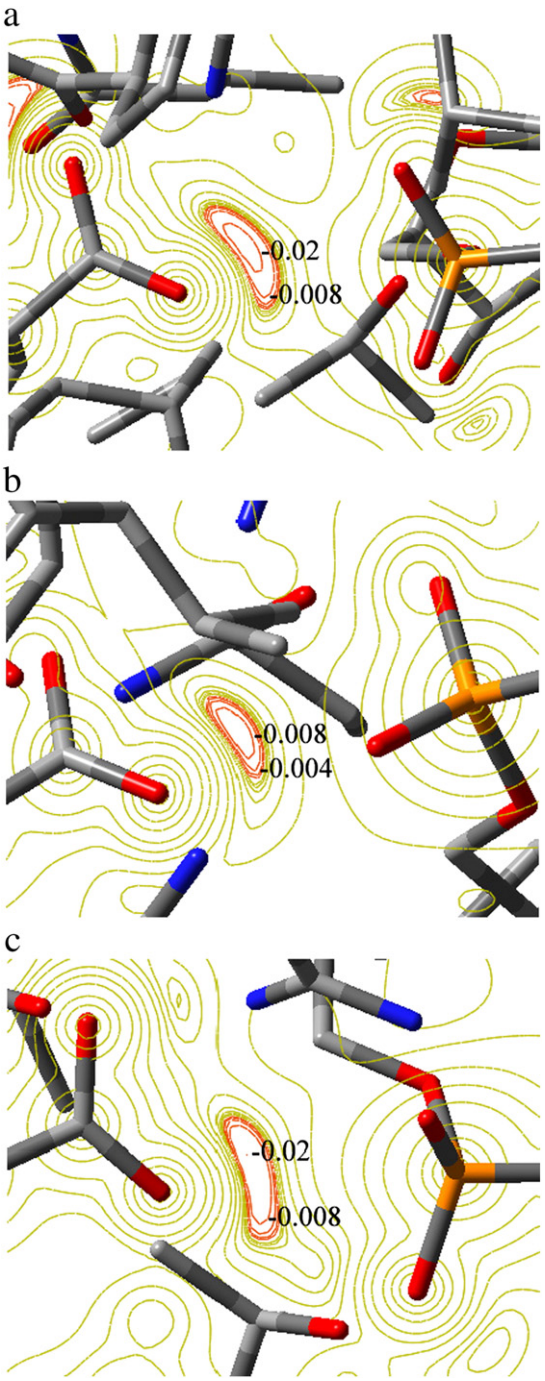

Fig. 9. Contour plot of the electrostatic potential for the optimized (a) $Model^{EC}_{Reactant(large)}$, (b) $Model^{TT}_{Reactant(large)}$ and (c) $Model^{SA}_{Reactant(large)}$ using HF/6-31G* level of theory. The range of the electrostatic potential is considered as ± 20 au. The Cartesian coordinates of the optimized models are given in Tables S2 (a–c) of the supporting information, respectively.

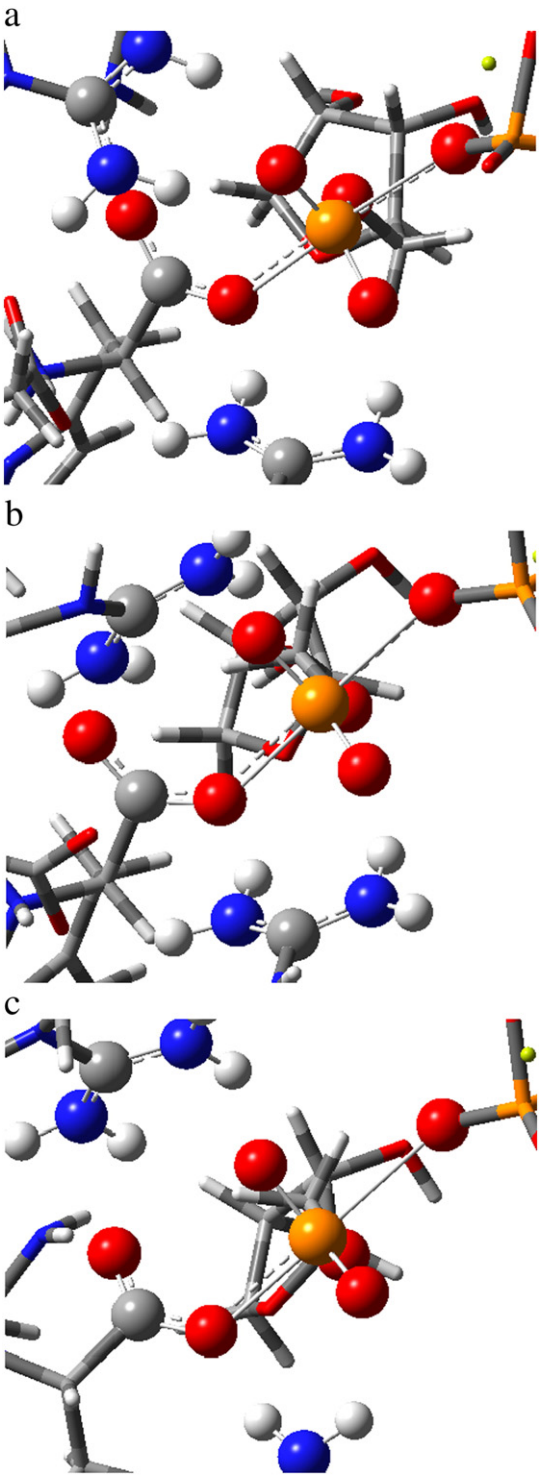

Fig. 10. The optimized geometries of the transition state of (a) EC, (b) TT and (c) SA of the activation step of aminoacylation reaction using two level ONIOM (HF/6-31G*:PM3//MP2/6-31G*:PM3) method. Side chains of the active site residues in close proximity of the reactants such as Glu83, Arg113, Gln127 and Arg259 are included in the calculation. The details of the model are described in text. The Cartesian coordinates of the optimized $Model^{EC/TT/SA}_{TS}$ are given in the Tables S3 (b), S4 (b) and S5 (b) of the supporting information, respectively.

other orientations are not effective for the catalytic activity of the residue.

The foregoing results show that the progress of the aminoacylation reaction follows a common reaction pathway as shown in detail using QM/semi-empirical method of calculation for *EC*, *TT* and *SA*. The mechanism is critically dependent on the conserved active site residues in close proximity of the reactants, each of which performs a specific role [24]. Although the roles vary from catalyzing the reaction, reducing the unfavorable electrostatic charges to facilitate the reaction to the task of positioning of substrate in a suitable orientation for reaction these general role, are common in the three species. This is confirmed by the identical feature of the molecular mechanism in three species as shown here.

The present analysis does not imply that the overall structure of the enzyme is irrelevant in understanding the mechanistic issues of

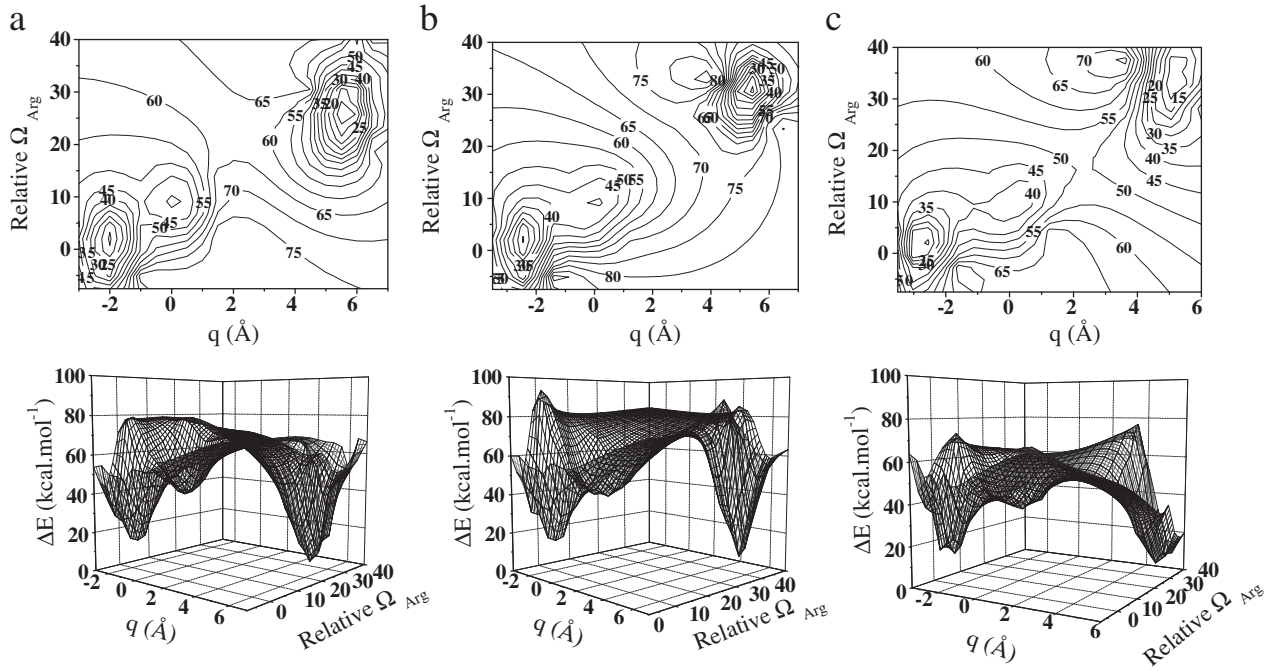

Fig. 11. Schematic representation of the contour (above) and three dimensional schematic representation of the energy surface (below) of the variation of energy in the reactant state, product state and the transition state for each of the (a) EC (b) TT and (c) SA respectively. The variation of interaction energy as a function of *q* (as discussed in the Section 2 and shown in Fig. 4) and relative orientation of the Arg259 is calculate at ONIOM (HF/6-31G*:PM3//HF/6-31G*:PM3) level of theory. The relative orientation of the Arg259 with respect to the His and ATP as present in the reactant state is taken as initial orientation (referred as zero degrees). The ΔE represents the relative energy in kcal.mol^{-1} with respect to the optimized product of the respective models. Cartesian coordinates of the optimized model used to generate these surfaces are given in the Tables S3, S4 and S5 of the supporting information.

the enzymatic reaction. While the overall enzyme structure influences the course of the reaction (due to the long range electrostatic influence of distant residues on the reactants located within active site), active site residues are closest to the substrate and have dominant influence on the course of the reaction. A distinction between the reaction chemistry and the catalytic mechanism is already pointed out in literature [17]. The reaction chemistry principally includes the overall strategy of changing the substrate into product, and the nature of the intermediates involved, whereas the catalytic mechanism describes the roles played by specific residues in the active site. Due to the remoteness of the positions of distant residues, they are unable to directly participate in the reaction mechanism. Hence, the active site residues in close proximity have more significant role in the reaction mechanism than the distant residues.

As mentioned in the Introduction section, the correlation between the conservation of active site residues in different species and the molecular mechanism of aminoacylation reaction is an unaddressed issue. The present study shows that conserved active site residues near the reaction center, which have role in the reaction mechanism and catalysis, retain their specific position and orientation relative to the substrate in different species. The resulting structural pattern of the active site is crucial for carrying out the reaction. While the features of the primary and secondary structures constituting the active site region are suggestive of this correlation, the energy profiles as a function of *q* and Ω_{Arg} and the ESP confirm that the structural pattern formed by conserved residues in *EC*, *TT* and *SA* have remarkable similarity. It is possible that these residues are conserved by evolution due to their indispensable role in carrying out the reaction efficiently. Detailed QM/semi-empirical analysis of the energy surfaces of reactant, transition state and product substantiates this view. The energy surfaces have close resemblance in three species and provide a clear perspective that how the reaction proceeds with the aid of different conserved residues. The present study is expected to be technologically significant for the development of designer active site templates for targeted peptide synthesis with high precision [44–50].

4. Conclusions

Summarizing, we first compared the primary and secondary structures of HisRS in *EC*, *TT* and *SA*. While the primary structures show both convergence and divergence, the secondary structure shows a considerable similarity in the organization of the respective active site structures. The structural arrangement indicates that the conserved active site residues near the reaction center, which have role in the reaction mechanism and catalysis, retain their specific position and orientation relative to the substrate in different species. The interactions are quantitatively analyzed using electronic structure based methods. First, a large model of active site with the substrates, Mg^{2+} ions and water is constructed in which the first shell residues near the reaction center are included. From the large model, a smaller model is constructed. Validation of the smaller model is carried out by comparing the energy surfaces of large and small models as a function of reaction coordinates. The ESP near the reaction center for the large and small model are further compared for validation. The reaction mechanisms as well as the electrostatic potentials near the respective reaction centers are analyzed for *EC*, *TT* and *SA*. The transition state structures of the activation step of aminoacylation reaction for *EC*, *TT* and *SA* are calculated using the combined *ab-initio*/semi-empirical calculation. The structural pattern of the conserved active site residues is thus shown to be vital for carrying out the reaction. The QM/semi-empirical analysis of the energy surfaces as a function of *q* and Ω_{Arg} related to the change from the reactant to the product via the transition state shows that the energy surfaces have close resemblance in the three species. The surfaces provide a clear perspective that how the reaction proceeds in identical manner in three different species with the aid of different conserved residues.

Acknowledgements

This work is supported by a grant from DST, India. S.D.B thanks University of Kalyani for a research scholarship.

Appendix A. Supplementary data

Supplementary data to this article can be found online at doi:10.1016/j.bpc.2011.05.006.

References

[1] M. Ibba, D. Söll, Aminoacyl-tRNA synthetases, Annu. Rev. Biochem. 69 (2000) 617–650.
[2] R. Sankaranarayanan, D. Moras, The fidelity of the translation of the genetic code, Acta Biochim. Pol. 48 (2001) 323–335.
[3] J.G. Arnez, D.C. Harris, A. Mitschler, B. Rees, C.S. Francklyn, D. Moras, Crystal structure of histidyl-tRNA synthetase from Escherichia coli complexed with histidyl-adenylate, EMBO J. 14 (1995) 4143–4155.
[4] R. Calendar, P. Berg, The catalytic properties of tyrosyl ribonucleic acid synthetases from Escherichia coli and Bacillus subtilis, Biochemistry 5 (1966) 1690–1695.
[5] J. Soutourina, P. Plateau, S. Blanquet, Metabolism of D-aminoacyl-tRNAs in Escherichia coli and Saccharomyces cerevisiae cells, J. Biol. Chem. 275 (2000) 32535–32542.
[6] F. Bergmann, P. Berg, M. Dieckmann, The enzymic synthesis of amino acyl derivatives of ribonucleic acid, J. Biol. Chem. 236 (1961) 1735–1740.
[7] S. Norton, J. Ravel, C. Lee, W. Shive, Purification and properties of the aspartyl ribonucleic acid synthetase of Lactobacillus arabinosus, J. Biol. Chem. 238 (1963) 269–274.
[8] T. Yamane, L. Miller, J.J. Hopfield, Kinetic proofreading: a new mechanism for reducing errors in biosynthetic processes requiring high specificity, Proc. Natl. Acad. Sci. U. S. A. 71 (1974) 4135–4139.
[9] K. Tamura, P. Schimmel, Chiral-selective aminoacylation of an RNA minihelix, Science 305 (2004) 1253.
[10] C.S. Francklyn, E.A. First, J.J. Perona, Y. Hou, Methods for kinetic and thermodynamic analysis of aminoacyl-tRNA synthetases, Methods 44 (2008) 100–118.
[11] G. Archontis, T. Simonson, D. Moras, M. Karplus, Specific amino acid recognition by aspartyl-tRNA synthetase studied by free energy simulations, J. Mol. Biol. 275 (1998) 823.
[12] S. Dutta Banik, N. Nandi, Orientation and distance dependent chiral discrimination in the first step of the aminoacylation reaction: integrated molecular orbital and semi-empirical method (ONIOM) based calculation, Coll. Surf. B Biointerface 74 (2009) 468–476.
[13] N. Nandi, Chiral discrimination in the confined environment of biological nanospace: reactions and interactions involving amino acids and peptides, Int. Rev. Phys. Chem. 28 (2009) 111–167.
[14] S. Dutta Banik, N. Nandi, Aminoacylation reaction in the histidyl-tRNA synthetase: fidelity mechanism of the activation step, J. Phys. Chem. B 114 (2010) 2301–2311.
[15] D. Thompson, C. Lazennec, P. Plateau, T. Simonson, Ammonium scanning in an enzyme active site the chiral specificity of aspartyl-tRNA synthetase, J. Biol. Chem. 282 (2007) 30856–30868.
[16] A. Warshel, P.K. Sharma, M. Kato, Y. Xiang, H. Liu, M.H.M. Olsson, Electrostatic basis for enzyme catalysis, Chem. Rev. 106 (2006) 3210–3235.
[17] A.E. Todd, C.A. Orengo, J.M. Thornton, Evolution of function in protein superfamilies, from a structural perspective, J. Mol. Biol. 307 (2001) 1113–1143.
[18] J. Gao, D.G. Truhlar, Quantum mechanical methods for enzyme kinetics, Ann. Rev. Phys. Chem. 53 (2002) 467–505.
[19] D.J. Wales, M.A. Miller, T.R. Walsh, Archetypal energy landscapes, Nature 394 (1998) 758–760.
[20] F.H. Stilinger, T. Weber, Packing structures and transitions in liquids and solids, Science 225 (1984) 983–989.
[21] S. Fischer, P.D.J. Grootenhuis, L.C. Groenen, W.P.van. Hoorn, F.C.J. vn van Veggel, D.N. Reinhoudt, M. Karplus, Pathways for conformational interconversion of calix[4]arenes, J. Am. Chem. Soc. 117 (1995) 1611–1620.
[22] V.L. Rath, L.F. Silvian, B. Beijer, B.S. Sproat, T.A. Steitz, How glutaminyl-tRNA synthetase selects glutamine, Structure 6 (1998) 439–449.
[23] G.P. Horsman, A.M.F. Liu, E. Henke, U.T. Bornscheuer, R.J. Kazlauskas, Mutations in distant residues moderately increase the enantioselectivity of pseudomonas fluorescens esterase toward methyl 3-bromo-2-methylpropanoate and ethyl 3-phenylbutyrate, Chem. Eur. J. 9 (2003) 1933–1939.
[24] J.G. Arnez, J.G. Augstine, D. Moras, C.S. Francklyn, The first step of aminoacylation at the atomic level in histidyl-tRNA synthetase, Proc. Natl. Acad. Sci. U. S. A. 94 (1997) 7144–7149.
[25] A. berg, A. Yaremchuk, M. Tukalo, B. Rasmussen, S. Cusack, Crystal structure analysis of the activation of histidine by Thermus thermophilus histidyl-tRNA synthetase, Biochemistry 36 (1997) 3084–3094.
[26] X. Qiu, C.A. Janson, M.N. Blackburn, I.K. Chhohan, M. Hibbs, S.S. Abdel-Meguid, Cooperative structural dynamics and a novel fidelity mechanism in histidyl-tRNA synthetases, Biochemistry 38 (1999) 12296–12304.
[27] D.L. Nelson, M.M. Cox, Lehninger Principles of Biochemistry, 4th ed. W.H. Freeman & Co., New York, 2002.
[28] J. Gao, Hybrid quantum and molecular mechanical simulations: an alternative avenue to solvent effects in organic chemistry, Acc. Chem. Res. 29 (1996) 298.
[29] D.G. Truhlar, J. Gao, C. Alhambra, M. Garcia-Vilosa, J. Corchado, M.L. Sanchez, J. Villa, The incorporation of quantum effects in enzyme kinetics model, Acc. Chem. Res. 35 (2002) 341.
[30] A. Gindulyte, A. Bashan, I. Agmon, L. Massa, A. Yonath, J. Karle, The transition state for formation of the peptide bond in the ribosome, Proc. Natl. Acad. Sci. USA 103 (2006) 13327–13332.
[31] F. Maseras, K. Morokuma, IMOMM: a new integrated ab initio + molecular mechanics geometry optimization scheme of equilibrium structures and transition states, J. Comp. Chem. 16 (1995) 1170.
[32] M. Svensson, S. Humbel, R.D.J. Froese, T. Matsubara, S. Sieber, K. Morokuma, ONIOM: a multilayered integrated MO + MM method for geometry optimizations and single point energy prediction. A test for Diels–Alder reactions and Pt(P(t-Bu)$_3$)$_2$ + H_2 oxidative addition, J. Phys. Chem. 100 (1996) 19357.
[33] T. Vreven, K. Morokuma, On the application of the IMOMO (integrated molecular orbital + molecular orbital) method, J. Comp. Chem. 21 (2000) 1419.
[34] H. Hu, W. Yang, Free energy of chemical reactions in solution and in enzymes with ab-initio quantum mechanics/molecular mechanics method, Annu. Rev. Phys. Chem. 59 (2008) 573–601.
[35] S. Dapprich, I. Komaromi, K.S. Byun, K. Morokuma, M.J. Frisch, A new ONIOM implementation in Gaussian98. Part I. the calculation of energies, gradient, vibrational frequencies and electric field derivatives, J. Mol. Struct. TheoChem 1–21 (1999) 461–462.
[36] J.J.P. Stewart, Optimization of parameters for semiempirical methods II applications, J. Comp. Chem. 10 (1989) 209–220.
[37] A.K. Rappi, C.J. Casewit, K.S. Colwell, W.A. Goddard III, W.M. Skid, UFF, a full periodic table force field for molecular mechanics and molecular dynamics simulations, J. Am. Chem. Soc. 114 (1992) 10024–10035.
[38] Q. Cui, H. Guo, M. Karplus, Combining ab initio and density functional theories with semi-empirical methods, J. Chem. Phys. 117 (2002) 5617–5631.
[39] S. Mietus, J. Tomasi, Approximate evaluations of the electrostatic free energy and internal energy changes in solution process, Chem Phys 65 (1982) 239–245.
[40] P. Sjoberg, P. Politzer, Use of the electrostatic potential at the molecular surface to interpret and predict nucleophilic processes, J. Phys. Chem. 94 (1990) 3959–3961.
[41] R. Bonaccorsi, E. Scrocco, J. Tomasi, Group contributions to the electrostatic molecular potential, J. Am. Chem. Soc. 98 (1975) 4049–4054.
[42] K.H. Hopmann, F. Himo, Insights into the reaction mechanism of soluble epoxide hydrolase from theoretical active site mutants, J. Phys. Chem. B 110 (2006) 21299–21310.
[43] M.J. Frisch, G.W. Trucks, H.B. Schlegel, G.E. Scuseria, M.A. Robb, J.R. Cheeseman, J.A. Montgomery Jr., T. Vreven, K.N. Kudin, J.C. Burant, J.M. Millam, S.S. Iyengar, J. Tomasi, V. Barone, B. Mennucci, M. Cossi, G. Scalmani, N. Rega, G.A. Petersson, H. Nakatsuji, M. Hada, M. Ehara, K. Toyota, R. Fukuda, J. Hasegawa, M. Ishida, T. Nakajima, Y. Honda, O. Kitao, H. Nakai, M. Klene, X. Li, J.E. Knox, H.P. Hratchian, J.B. Cross, V. Bakken, C. Adamo, J. Jaramillo, R. Gomperts, R.E. Stratmann, O. Yazyev, A.J. Austin, R. Cammi, C. Pomelli, J.W. Ochterski, P.Y. Ayala, K. Morokuma, G.A. Voth, P. Salvador, J.J. Dannenberg, V.G. Zakrzewski, S. Dapprich, A.D. Daniels, M.C. Strain, O. Farkas, D.K. Malick, A.D. Rabuck, K. Raghavachari, J.B. Foresman, J.V. Ortiz, Q. Cui, A.G. Baboul, S. Clifford, J. Cioslowski, B.B. Stefanov, G. Liu, A. Liashenko, P. Piskorz, I. Komaromi, R.L. Martin, D.J. Fox, T. Keith, M.A. Al-Laham, C.Y. Peng, A. Nanayakkara, M. Challacombe, P.M.W. Gill, B. Johnson, W. Chen, M.W. Wong, C. Gonzalez, J.A. Pople, Gaussian 03, revision C.02, Gaussian, Inc, Wallingford, CT, 2004.
[44] D.E. Benson, M.S. Wisz, H.W. Hellinga, Rational design of nascent metalloenzymes, Proc. Natl. Acad. Sci. USA 97 (2000) 6292–6297.
[45] E. Pérez-Payá, R.A. Houghten, S.E. Blondelle, Functionalized protein-like structures from conformationally defined synthetic combinatorial libraries, J. Biol. Chem. 271 (1996) 4120–4126.
[46] J.W. Bryson, S.F. Betz, H.S. Lu, D.J. Suich, H.X. Zhou, K.T. O'Neil, W.F. DeGrado, Protein design: a hierarchic approach, Science 270 (1995) 935–941.
[47] S. Kamtekar, J. Schiffer, H. Xiong, J. Babik, M. Hecht, Protein design by binary patterning of polar and nonpolar amino acids, Science 262 (1993) 1680–1685.
[48] S. Benner, Catalysis: design versus selection, Science 261 (1993) 1402–1403.
[49] T. Handel, S. Williams, W. DeGrado, Metal ion-dependent modulation of the dynamics of a designed protein, Science 261 (1993) 879–885.
[50] H. Xiang, L. Luo, K.L. Taylor, D. Dunaway-Mariano, Interchange of catalytic activity within the 2-enoyl-coenzyme A hydratase/isomerase superfamily based on a common active site template, Biochemistry 38 (1999) 7638–7652.
[51] W. Humphrey, A. Dalke, K. Schulten, VMD: visual molecular dynamics, J. Mol. Graph. 14 (1996) 33–38.